FULL ARTICLE





Investigation of the source-detector separation in near infrared spectroscopy for healthy and clinical applications

Lei Wang^{1*}

Hasan Ayaz^{1,2,3}

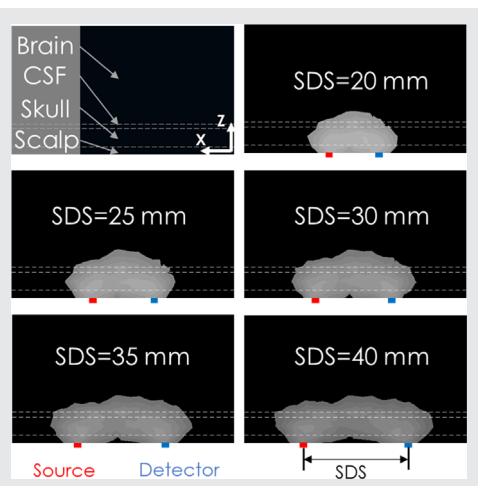
Heltem Izzetoglu⁴

*Correspondence

Lei Wang, Drexel University, School of Biomedical Engineering, Science and Health Systems, Philadelphia, PA, 19104. Email: lw474@drexel.edu

Abstract

Understanding near infrared light propagation in tissue is vital for designing next generation optical brain imaging devices. Monte Carlo (MC) simulations provide a controlled mechanism to characterize and evaluate contributions of diverse near infrared spectroscopy (NIRS) sensor configurations and parameters. In this study, we developed a multilayer adult digital head model under both healthy and clinical settings



and assessed light-tissue interaction through MC simulations in terms of partial differential pathlength, mean total optical pathlength, diffuse reflectance, detector light intensity and spatial sensitivity profile of optical measurements. The model incorporated four layers: scalp, skull, cerebrospinal-fluid and cerebral cortex with and without a customizable lesion for modeling hematoma of different sizes and depths. The effect of source-detector separation (SDS) on optical measurements' sensitivity to brain tissue was investigated. Results from 1330 separate simulations [(4 lesion volumes \times 4 lesion depths for clinical +3 healthy settings) \times 7 SDS \times 10 simulation = 1330)] each with 100 million photons indicated that selection of SDS is critical to acquire optimal measurements from the brain and recommended SDS to be 25 to 35 mm depending on the wavelengths to obtain optical monitoring of the adult brain function. The findings here can guide the design of future NIRS probes for functional neuroimaging and clinical diagnostic systems.

KEYWORDS

www.biophotonics-journal.org

hematoma, Monte Carlo simulation, multi-layer digital brain model, near infrared spectroscopy (NIRS), source-detector separation (SDS)

1 | INTRODUCTION

Near infrared spectroscopy (NIRS) is a light-based noninvasive technology used to monitor regional tissue oxygen

status [1]. It is widely deployed in medicinal plants, foods, pharmaceutical and biomedical applications combined with imaging studies [2] and also as a neuroimaging modality that allows noninvasive investigation of brain tissue oxygenation

¹Drexel University, School of Biomedical Engineering, Science and Health Systems, Philadelphia, Pennsylvania

²Department of Family and Community Health, University of Pennsylvania, Philadelphia, Pennsylvania

³Children's Hospital of Philadelphia, Center for Injury Research and Prevention, Philadelphia, Pennsylvania

⁴Villanova University, Electrical and Computer Engineering, Villanova, Pennsylvania

and brain function [3-7]. NIRS use for neuroimaging is based on the fact that human tissues are relatively transparent to light in the near infrared spectral window (650-1000 nm), and light can either be absorbed by pigmented compounds (chromophores) or scattered in tissues, where oxy-hemoglobin (HbO) and deoxy-hemoglobin (HbR) are generally considered as dominant absorbers [4]. There is an increase in oxygen consumption during brain activation, which is accompanied by an increase in cerebral blood flow due to neurovascular coupling, and leads to a change in local HbO and HbR concentrations [8]. These changes can then be encoded in the light and captured by detector.

In order to investigate the propagation path of the detected signal in biological tissues, several theoretical and experimental studies have been performed in various head models [9–12]. Analytical solutions to radiative transport equation (RTE) through diffusion approximation is one way to study light-tissue interaction [13]. However, many approximations and assumptions are required to achieve such analytical solutions, which hinder the use of these methods in realistic situations and real-life conditions. The Monte Carlo (MC) method is a more typically employed numerical technique in recent studies [14–18]. MC method is based on simulation of a large number of random photon trajectories where the shape of each trajectory depends on the absorption and scattering properties of the tissues [19]. Since MC effectively solves the RTE via random sampling and does not need to assume an analytical form for photon propagation, it offers excellent accuracy when simulating photon propagation inside a complex medium [10, 20]. In many cases, MC was chosen as the gold standard when validating new algorithms or approximations [21]. MC has several additional merits such as being easy to program, and it is straightforward to parallelize [11]. Compared with finite element (FE) diffusion equation solvers used in many diffuse optical imaging applications, MC produces more accurate solutions, especially when simulating low scattering media where the diffusion approximation becomes invalid [11, 22]. One of the drawbacks of MC is its low computational efficiency; for example, a traditional MC simulation can easily take several hours or even over a day to obtain a solution with the desired accuracy.

A number of groups have used MC methods to investigate different source-detector separation (SDS) values in layered tissues [9, 10, 23–26]. The ideal SDS was suggested to be designed within 20 to 30 mm, 30 to 35 mm, or an even larger range, with the premise that the instrument can provide adequate signal-to-noise ratio (SNR) at those separations. SDS had also been discussed in depth in some other experimentally dominated researches. Kohri et al. advised SDS to be greater than 20 mm in conventional non-timeresolved measurements for detecting the hemodynamic changes in cerebral tissue of the adult human head [27]. Gratton et al. suggested SDS to be at least 22.5 mm in detecting the fast optical signal of brain activity [28], while Li et al. recommended the optimal SDS to be narrowed down to 30 to 35 mm [29]. Recently, Herold et al. proposed the SDS to be sufficiently large to adequately assess cortical blood flow, with a minimum distance of 30 mm [30]. Some other groups also supported SDS to be 30 mm [31, 32] or 40 mm [33]. All these studies have provided valuable insights; however, the selection of SDS in NIRS sensor configuration remains controversial, considering the range of 15 to 45 mm is commonly adopted in different studies using lab-built or commercially available devices [8, 30, 34–37]. More importantly, all these studies were performed on head models for healthy applications, and no head model for clinical applications were taken into consideration in SDS targeted investigation.

Numerous applications of NIRS technology in the assessment of brain function under various clinical conditions caused by traumatic brain injury (TBI) or stroke indicate the importance of study and evaluation of light tissue interaction under such conditions [3, 6, 38-42]. Applying various types of clinically relevant changes in the brain such as intracranial hematoma development on a digital model could effectively help in predicting the photon path during measurements with a NIRS device, improving the diagnosis of brain injury. However, the study of MC simulations on an injured brain in the literature is scarce. To the best of our knowledge, there is only one study that investigated light-tissue interaction in an injured brain though MC simulation [43]. However, we intend to fully investigate clinical cases such as intracranial hemorrhage.

In this study, our aim is to indicate an optimal SDS range for NIRS monitoring of adult brain function for healthy and clinical applications. To do so, we have run MC simulations in a digital phantom with and without cerebral hematomas. We introduced different system measures calculated from MC simulation, such as absolute sensitivity, proportional sensitivity, detected light intensity and spatial sensitivity profile, and then evaluated these measures at various SDS. We then recommended an ideal SDS range for probe design in adult brain function measurement. The detailed quantitative information provided in this study can help investigators to better select an appropriate probe distance for their applications.

2 | METHOD

2.1 | Adult head digital phantom

The human head is a heterogenous medium, which consists of scalp, skull, cerebrospinal fluid (CSF) and brain tissue

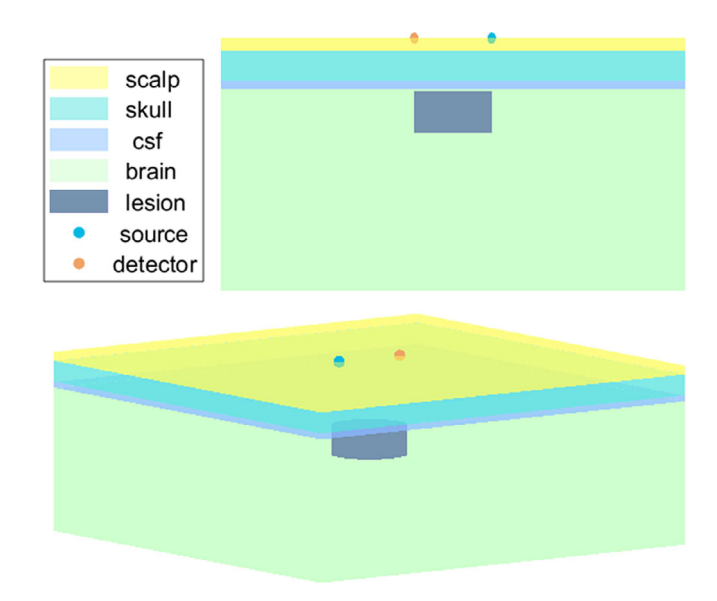


FIGURE 1 Geometry of four-layer slab digital phantom for MC simulation

(gray matter and white matter). A three-dimensional digital phantom with four-layer slab geometry ($150 \times 150 \times 60 \text{ mm}^3$) was designed to model the adult head as illustrated in Figure 1. The thickness of each layer was designed as: 3 mm of scalp, 7 mm of skull, 2 mm of CSF and the rest brain tissue [43]. Seven different SDS were adopted: 10, 15, 20, 25, 30, 35 and 40 mm. The light detector was modeled as a disk with a radius of 1.29 mm, according to previous investigation of detector surface area [37].

A cerebral hematoma, modeled as a 10-mm-high cylinder, was placed at a 0.5 mm depth within the brain layer. The lesion was located at the midline between source and detector, and increased in radius (9.77, 12.62, 17.84 and 30.90 mm), resulting in 3, 5, 10 and 30 cc lesion volumes, chosen to cover a range of intracranial hematomas. Optical properties assigned to each tissue type for MC simulation are as shown in Table 1, representing tissue optical characteristics under 690 nm wavelength [37, 44].

Previous investigations had confirmed that NIRS measurements can be affected by skull thickness [45], considering that the thickness of skull varies with age and head positions [46]. For the digital head model under healthy setting, the thickness of the skull was further altered to 4, 7 and 10 mm [12] to evaluate the effect of skull thickness on system measures across various SDS ranges.

TABLE 1 Tissue optical properties in digital head phantom. Anisotropy g = 0.9 and refractive index n = 1.4 in all tissues

	Scalp	Skull	CSF	Brain	Hematoma
$\mu_a~(mm^{-1})$	0.0162	0.0103	0.0004	0.0182	0.50
$\mu_s \ (mm^{-1})$	7.87	9.83	0.10	12.29	7.25

2.2 | MC simulation

We employed a Mesh-based MC (MMC) method, based on the code described by Fang [11], with the general approach described by Wang et al. [18] MMC utilizes a tetrahedral mesh to model a complex anatomical structure. Ten simulations were run for each SDS per model case, where 100 million size photon packets were launched from the light source. MMC is able to compute the partial pathlength of each photon per layer, based on predefined SDS and detector surface area. Then, the mean total optical pathlength (MPL), partial differential pathlength (PPL, also called absolute sensitivity), diffuse reflectance and proportional sensitivity (or relative sensitivity) were calculated [17]. The simulations were run on the hardware supported by Drexel's University Research Computing Facility.

In MC simulation, the received intensity of any given photon will be attenuated by a factor of $\exp(-\mu_{ai}L_i)$ for any non-zero attenuation in tissue i, where μ_{ai} is the absorption coefficient of tissue i, L_i is the pathlength traveled by a single output photon within tissue i and is calculated by accumulating the scattering length in each medium. Thus, the weight W^i of an exit photon i is

$$W^{j} = W_{0} \prod_{i} \exp\left(-\mu_{ai} L_{i}^{j}\right) \tag{1}$$

where initial survival weight W_0 is set to 1 and initial position and direction of a photon are defined as coming from a point source [10, 17, 47]. With a large number of photons captured by a detector, the PPL of layer i is calculated as [17]

$$PPL_i = \sum_{j} (L_i^j W^j) / \sum_{j} W^j$$
 (2)

 PPL_i represents the absolute sensitivity to an absorption change in tissue layer i [48]. Then the MPL can be obtained by

$$MPL = \sum_{i} PPL_{i}$$
 (3)

Given MPL and PPL_i, the relative sensitivity, which is the proportion of the total NIRS signal change that derives from a given layer, can be defined as follows: [48]

Proportional Sensitivity =
$$PPL_i/MPL$$
 (4)

Diffuse reflectance, as a measurement about the reflection of light from a surface that photons are scattered at many angles, was also calculated.

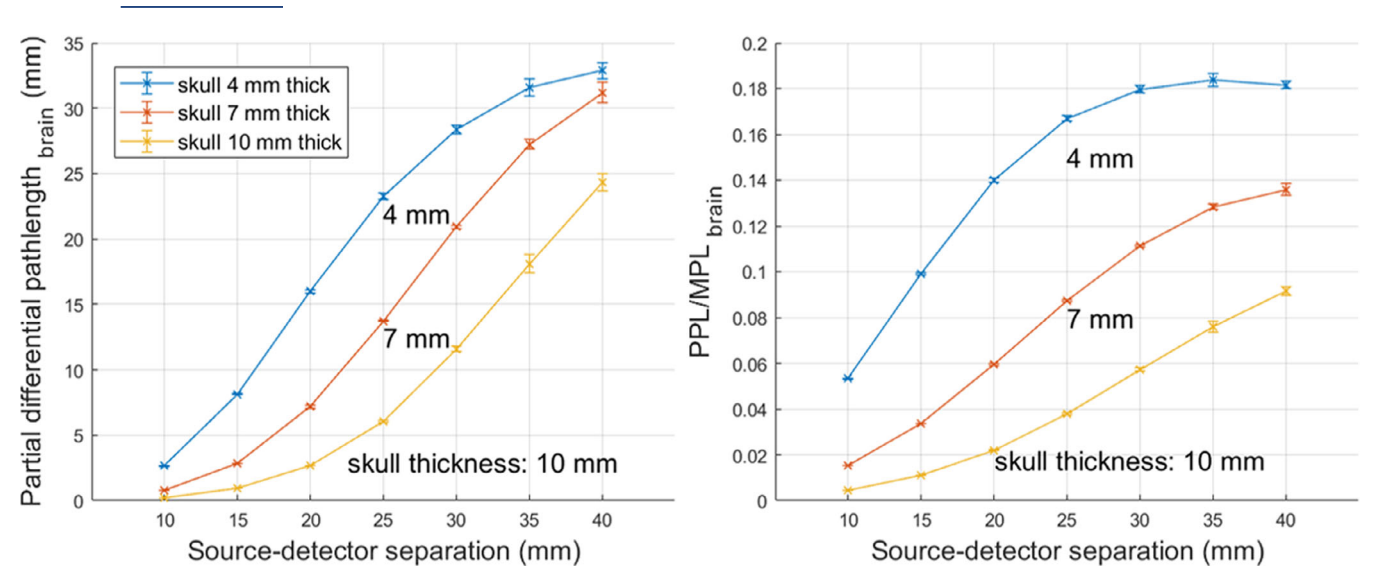


FIGURE 2 Mean absolute sensitivity (left) and proportional sensitivity (right) to brain for an adult head model as a function of SDS predicted by MC simulation for different skull thicknesses. Error bar represent SD of 10 random simulations

3 | RESULTS

3.1 | Absolute and proportional sensitivity

The computed absolute sensitivity (PPL_i) and proportional sensitivity (PPL_i/MPL) to brain tissue of the adult head model under healthy setting were plotted against SDS in Figure 2. Notably, as skull thickness increased, both sensitivities to brain decreased. The relationship between absolute sensitivity and the thickness of the skull is almost linear when SDS is 25 and 30 mm. In absolute sensitivity curves, when SDS became greater than 30 mm, the difference between the curves of different models turns out to be larger as skull thickness increased from 4 mm, 7 mm to 10 mm, see also in Figure S1.

The proportional sensitivity to brain tissue is almost the same value as the SDS within the range from 30 to 40 mm for the model with a 4-mm-thick skull, around 18%. With an increase in skull thickness, the decrease in proportional sensitivity to brain became smaller. In the case of SDS = 25 mm, the model with a 4-mm-thick skull had more than four times the proportional sensitivity to brain compared with the model with a 10-mm-thick skull and is about more than two times in the case of SDS = 40 mm. For the uninjured brain model, with the increase in SDS, both absolute sensitivity and proportional sensitivity to brain increased, and curves became flatter as SDS gradually increased. However, the measurement was substantially more sensitive to the extra cerebral tissues (scalp, skull and CSF) than brain tissue, see also in Figure S2.

3.2 | Reflectance and light intensity

Diffuse reflectance curves of injured head model with 7-mm-thick skull in Figure 3 (left) indicated that there is an

optical density difference between the uninjured brain and injured brain when the SDS was greater than 20 mm. When the hematoma was 0.5 mm away from the CSF in brain tissue, the 3 cc hematoma was slightly distinguishable as the diffuse reflectance profile began to separate from no lesion profile, and a 50 cc hematoma was clearly distinguishable from the baseline (uninjured) condition. The larger the SDS, the more distinguishable the curves of injured brain from uninjured brain. Here, contrast was defined as the difference in reflectance between the uninjured brain model (baseline) and injured brain model, divided by baseline value [43]. In Figure 3 (right), contrast increased as SDS increased, the model with relatively larger volume of hematoma achieved higher contrast value, and curves became flatter in general as SDS increased.

The intensity of detected light predicted by MC simulation on the uninjured brain model is shown in Figure 4. The results were normalized by the intensity of incident light. The detected intensity slowly decreased with an increase in skull thickness, and the slope increased with an increase in SDS. The detected intensity decreased with an increase in SDS. It decreased about 10 times from SDS = 10 to SDS = 15 mm, whereas there was only about a 2 times reduction from SDS = 35 to SDS = 40 mm.

3.3 | Spatial sensitivity profile

The MC simulated spatial sensitivity profiles of an uninjured head model with 7-mm-thick skull at different SDS are displayed in Figure 5. Contour lines appeared at each order of magnitude decrease in the photon sensitivity profile from the peak element, then were truncated in each figure after decaying five orders of magnitude. When SDS was shorter

18640648, 2019, 11, Downloaded from https

//onlinelibrary.wiley.com/doi/10.1002/jbio.201900175 by Drexel University, Wiley Online Library on [19/12/2023]. See the Terms and Conditions (https://onlinelibrary.wiley.com/

onditions) on Wiley Online Library for rules of use; OA articles are governed by the applicable Creative Commons License

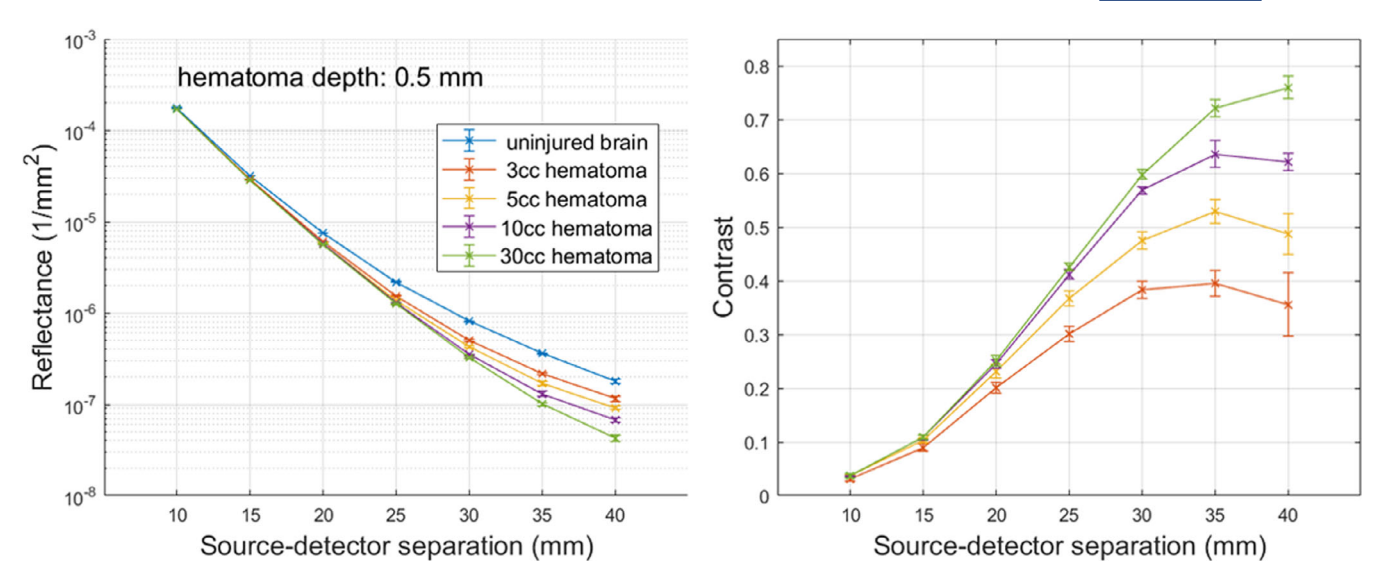


FIGURE 3 Spatially resolved diffuse reflectance (left) and contrast (right) calculated by MC simulation of adult head model with 7-mm-thick skull. Error bar represent SD of 10 random simulations

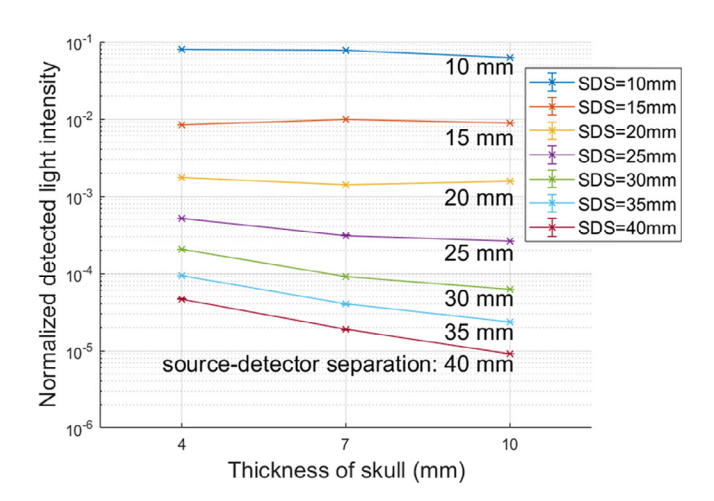


FIGURE 4 Normalized intensity of detected light as a function of skull thickness predicted by MC simulation. Error bar represent SD of 10 random simulations

than 20 mm, the spatial sensitivity profiles were confined to the superficial layers (scalp, skull and CSF layers). As SDS increased from 10 to 20 mm, the banana-shaped path grew and extended deeper into the brain. When SDS increased from 25 to 40 mm, the spatial sensitivity profiles shifted deeper into the brain layer [47], and the penetration depth barely changed, staying around 18 mm of the model (about 6 mm depth of brain tissue layer). It is notable that the larger the SDS, the more sensitivity to brain tissue increased, whereas the profile gray level decreased.

Similarly, Figure 6 shows vertical spatial sensitivity profiles (view of midline plane between source and detector) of the same model at different SDS. As SDS increased from 10 to 40 mm, in addition to the gray level decrease and

sensitivity profile shift to the brain layer, which was the same as in Figure 5, the sensitivity profiles also extended to a wider spread in both Figures 5 and 6.

The spatial sensitivity profiles of the uninjured head model with skull thickness varied in 4, 7 and 10 mm at SDS of 25, 30, 35 and 40 mm are shown in Figure 7. The most intense region of the spatial sensitivity profile in the *x-y* plane in the brain was reduced and was more concentrated at the midpoint of the source and detector with an increase in skull thickness [12]. Profiles for SDS smaller than 25 mm are shown in Figure S9.

Figure 8 illustrates the spatial sensitivity profile of the injured head model with 7-mm-thick skull and a 5 cc hematoma presented at 0.5 mm deep in the brain tissue layer. When SDS was shorter than 20 mm, the spatial sensitivity profile was strictly confined to non-brain tissue. When SDS increased larger than 20 mm, the sensitivity profile shifted to the deeper level and extended wider within brain tissue. Similar to the uninjured head model, the detected light intensity declined with an increase in SDS.

4 | DISCUSSION

In this article, we utilized a set of MC simulations on fourlayer slab geometry adult head model under healthy and clinical settings to assess the optical measurements with different SDS. Overall, the sensitivity was found to be strongly variable with different SDS of the ranges investigated. Different system measures as a function of SDS were qualitatively consistent with previous reports [10, 25, 26, 48, 49]. With increasing SDS, detected light intensity (signal strength) decreased. However, proportional sensitivity to

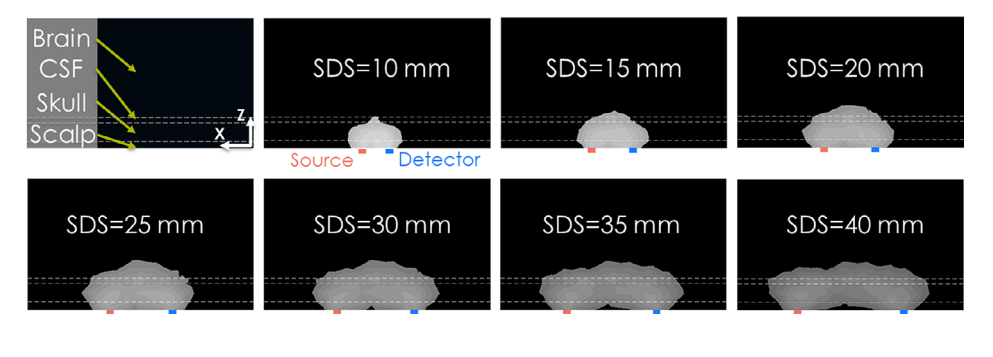


FIGURE 5 Spatial sensitivity profile in *x-z* plane of 7-mm-thick skull uninjured head model at a range of SDS. Contours are drawn for each order of magnitude loss in sensitivity from peak and are truncated after five orders of magnitude

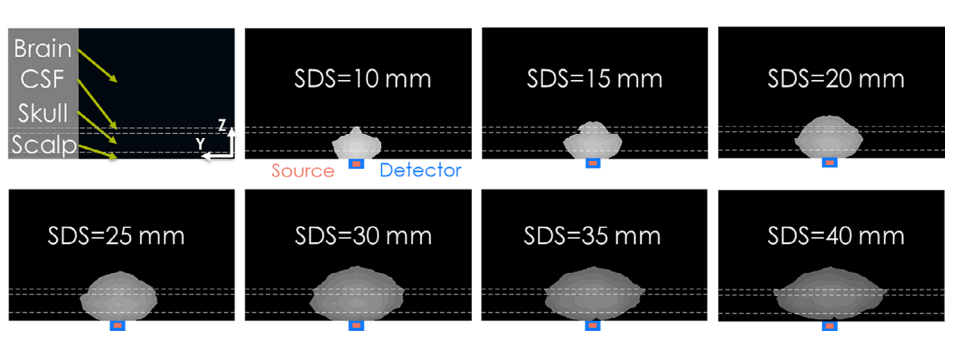


FIGURE 6 Spatial sensitivity profile in *y-z* plane of 7-mm-thick skull uninjured head model at a range of SDS, view of midline plane between source and detector. Contours are drawn for each order of magnitude loss in sensitivity from peak and are truncated after five orders of magnitude

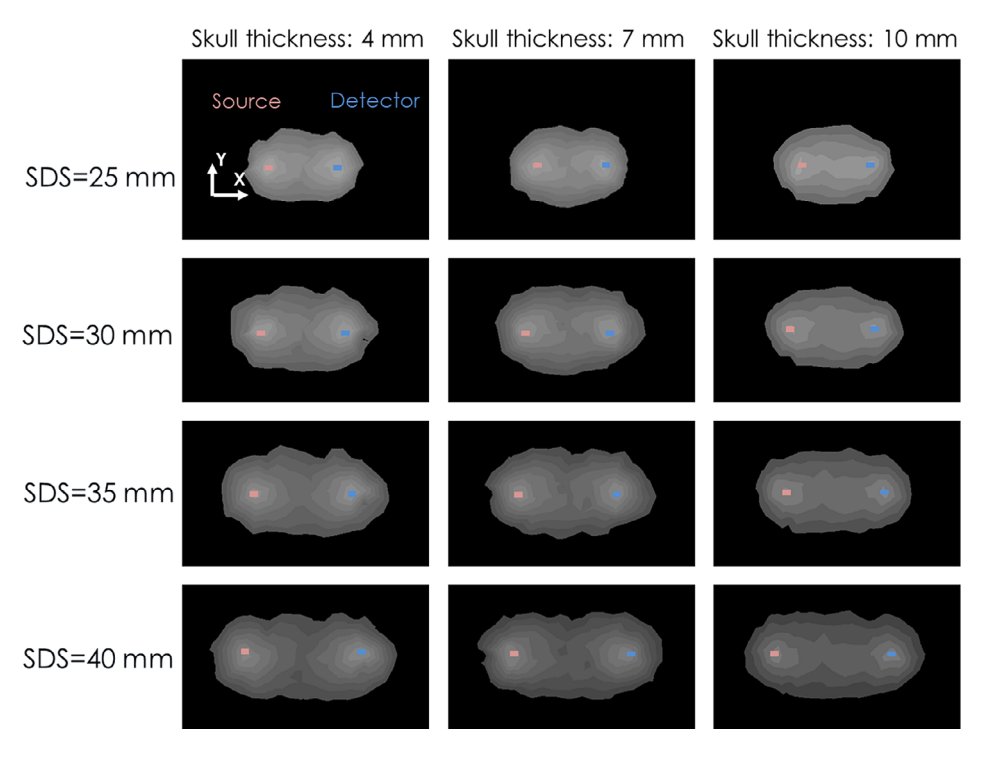
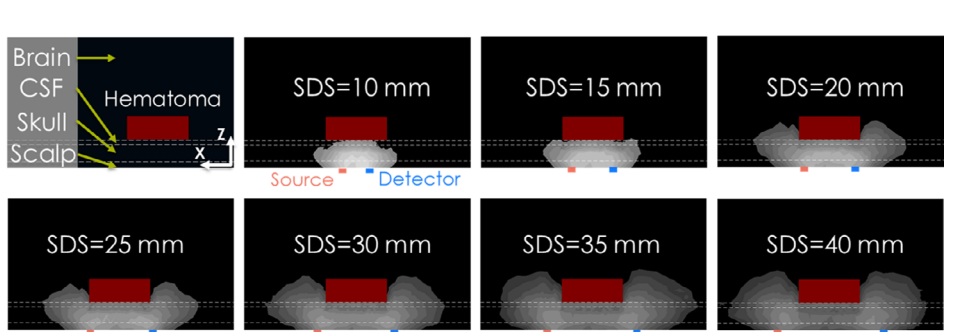


FIGURE 7 Spatial sensitivity profile in *x-y* plane of uninjured head model at SDS = 25, 30, 35 and 40 mm, view of bottom plane on source and detector. Contours are drawn for each order of magnitude loss in sensitivity from peak and are truncated after seven orders of magnitude



profile in *x-z* plane of 7-mm-thick skull head model with 5 cc hematoma at 0.5 mm deep in brain layer at different SDS. Contours are drawn for each order of magnitude loss in sensitivity from peak and are truncated after seven orders of magnitude

brain tissue increased with an increase in SDS, the highest around 18%, while non-brain tissue possessed the remaining part. Penetration depth barely changed after SDS was greater than 25 mm where the width of penetrated light increased as SDS increased. When lesions such as cerebral hematoma were present within brain tissue, observed signals started to distinguish injured brain from the uninjured brain when SDS was greater than 20 mm.

4.1 | Sensitivity to brain tissue

An increase in brain sensitivity was expected with larger SDS [10, 17, 25, 47]. Considering the thickness of the skull layer varies with location on the adult head, results of proportional sensitivity revealed that sensitivity to brain tissue can be 18% at SDS = 40 mm, which is higher than sensitivity to brain at smaller SDS. Also, sensitivity to non-brain tissue dropped as SDS increased. The greater the SDS, the greater the effect of skull thickness was on the sensitivity to brain, see also in Figures S1 and S2.

Careful visual inspection of examples in spatial sensitivity profiles also revealed that the relatively non-scattering CSF layer distorted the normally smooth ovoid structure of the NIRS banana-shaped path that is found in a homogeneous medium [10, 12, 49]. Such distortion was particularly noticeable when SDS became larger (see also the spatial sensitivity profile of model with 4-mm-thick skull in Figures S5 and S6 and profile of model with 10-mm-thick skull in Figures S7 and S8). The profile contours also suggested that there was at least limited sensitivity to brain tissue at SDS less than 20 mm, since those separations are typically assumed to provide almost zero sensitivity to brain in both uninjured brain [10] and injured brain model.

Thus, in order to gain more access to brain tissue instead of non-brain tissue (scalp, skull and CSF), a larger SDS should be implemented. However, despite the relatively higher sensitivity to brain tissue, the signal strength and SNR should also be considered in selecting SDS in NIRS measurement.

4.2 | Detected light intensity

Signal strength, that is, the intensity of detected light, drops significantly with an increase in SDS, which was also confirmed in previous reports [19, 47, 49, 50]. Our MC simulation results showed that the intensity of detected light dropped linearly over SDS ranging from 10 to 20 mm. Beyond 20 mm, further SDS increases continued to reduce detected light intensity relatively linearly, but with smaller slope. Reduced signal strength with increasing SDS was also reflected in the spatial sensitivity profile. In the spatial sensitivity profile, the penetration depth of light into the brain

tissue was almost the same as SDS as it increased above 25 mm, which is greater than that observed from smaller SDS. The further apart the source and detector, the darker the peak element of each example became, which indicated reduced signal strength.

Increasing SDS resulted in a reduction in SNR [23, 47], as shown in Figure 9. SNR values were acquired from absolute sensitivity, proportional sensitivity and normalized light intensity, simulated on the uninjured head model with skull thickness varied in 4, 7 and 10 mm. There was a statistically significant difference between SDS as determined by oneway ANOVA (F (6, 56) = 4.755, p = .001). A Tukey posthoc test revealed that the SNR was significantly lower when SDS increased to 35 mm (38.43 \pm 7.02 dB, p = .003) and 40 mm $(38.16 \pm 5.89 \text{ dB}, p = .003)$ compared to $SDS = 10 \text{ mm} (52.53 \pm 9.48 \text{ dB}) \text{ and } SDS = 15 \text{ mm}$ $(49.66 \pm 7.40 \text{ dB})$. There was no statistically significant difference between other SDS groups. SNR obtained from MC simulation might be optimistic compared to experimental conditions where other instrumental sources of noise, such as background noise arising from dark counts and stray light, deteriorate the signal [51]. The situation would be even worse for longer SDS.

Results about light intensity and SNR reveal that in order to obtain reliable signal in NIRS measurements, too large SDS should be avoided. From SDS = 20 to SDS = 40 mm, the decline in detected light intensity and hence decrease in SNR was more pronounced than the increase in sensitivity to brain [47]. Moreover, relatively thicker skull tissue also contributed to a faster decline in intensity in the spatial sensitivity profile. Thus, with the aim of reaching a balance or trade-off between light intensity and sensitivity to brain tissue, SDS in NIRS probes for adult brain function monitoring should be carefully selected to be within 25 to 35 mm. The

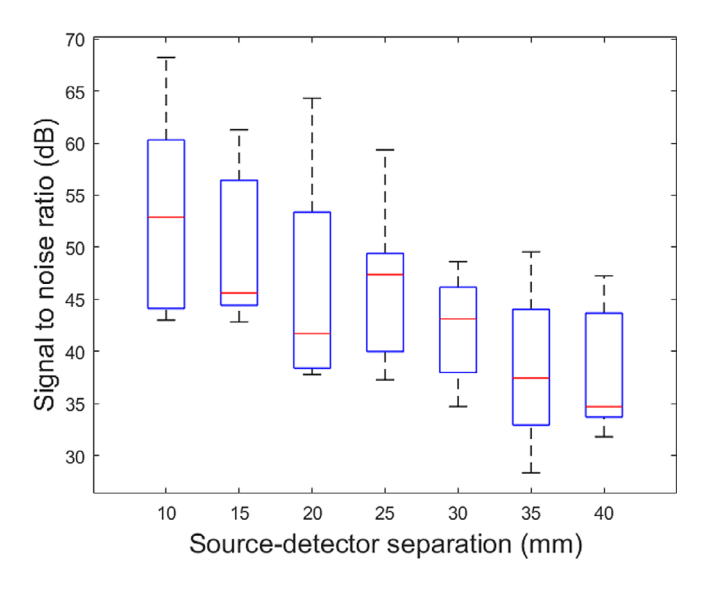


FIGURE 9 SNR as a function of SDS

recommendation should also be weighed according to wavelength selection and spatial resolution when choosing SDS,

4.3 | Multidistance probing

as Strangman et al. suggested [10].

For larger SDS, detected light intensity is relatively lower than that of the recommended range, which might be compensated for by increasing the power of the light sources used in the device. However, this operation may raise safety issues and also does not ensure measured optical density with sufficient SNR [52]. For smaller SDS, non-brain tissue contributed to the relatively larger proportion of the sensitivity, resulting in almost zero sensitivity to brain. This finding is one of the reasons that some studies suggested using multiple SDS pairs to measure brain function accurately [53–57] where short SDS (e.g. 5, 10, or 15 mm) was implemented along with long SDS (e.g. 30 or 40 mm) to measure and remove contributions of extracerebral tissue.

For SDS shorter than 20 mm, our spatial sensitivity profiles on x-z and y-z planes did display profiles restricted to superficial layers where each profile was drawn according to each order of magnitude decrease from peak element. However, upon close inspection of proportional sensitivity with shorter SDS, we found that when SDS = 10 mm, the PPL of these photons traveled created around 2% sensitivity to brain tissue over total MPL; when SDS = 15 mm, proportional sensitivity was 3%. These findings indicated that shorter SDS such as 10 and 15 mm did measure brain tissue, though with relatively minor contribution and higher signal strength. Considering the fact that skull thickness can vary at different head locations and by age, which in turn affects the sensitivity to brain tissue, careful analysis on the selection of multidistance SDS should be carried out. Our results indicated that proportional sensitivity from the 4-mm-thick skull model is about 10 times more than that from 10-mm-thick skull model with shorter SDS (10 and 15 mm). Hence, when applying multidistance probe NIRS measurements of brain function, the positioning of the short and long SDS pair [58] can be as important as the selection of precise algorithms to remove noise from superficial layers. Furthermore, for infant or child head models, sensitivity to brain might be even higher than that of the adult head model for each SDS; therefore, the selection of SDS pairs in such younger populations should be performed with more caution.

4.4 | NIRS ability to detect cerebral hematoma

Based on the results from the injured head model with 7-mm-thick skull for hematoma of different sizes at 0.5 mm depth, diffuse reflectance and spatial sensitivity profiles

further confirmed that the SDS should be at least 25 mm, since there is no optical density difference between uninjured brain and injured brain when SDS is smaller than 25 mm, and spatial sensitivity profile was confined to extracerebral tissues below this SDS range. As SDS increased, contrast to baseline level increased, and hematoma with larger volumes also reached higher contrast values. At the presence of hematoma, the high absorption of blood within the hematoma made it harder for photons to pass through to the brain tissue and resulted in higher sensitivity to superficial layers. NIRS products available in market have been tested to prove the ability to detect cerebral hematoma [41, 42, 59–61], all with SDS greater than 25 mm.

We further simulated an injured head model with lesions present at even deeper locations in brain tissue: 3, 5.5 and 8 mm, with results shown in Figures S3 and S4. With lesions located deeper within brain tissue, NIRS measurements were not able to distinguish different volumes of lesions. When lesions were displayed at 5.5 and 8 mm deep within bran tissue layer, diffuse reflectance cannot distinguish uninjured brain from injured brain having hematoma of any size. This result indicated that for SDS range from 10 to 40 mm, the depth that photons can reach into injured brain tissue is less than 5.5 mm.

4.5 | Other aspects

In our previous study, which evaluated the detector surface area as a critical system parameter in minimizing the error in concentration calculation, we concluded that when the detector radius was a fixed value, DPF became unstable with increasing SDS [37]. DPF is a scaling factor indicating how many times longer than SDS the detected light can travel within the tissue, which is an important NIRS system parameter used in modified Beer–Lambert law (MBLL) conversion to obtain chromophore concentrations. When the detector surface area was a constant value, DPF had a larger variation at SDS = 40 mm as compared to shorter SDS range, which was more pronounced when detector areas were smaller [37]. Thus, to reduce the error in concentration calculation, SDS should not be selected as too large, especially for smaller detector areas.

The spatial sensitivity profiles reported in this article have also revealed that a relatively greater lateral spread can be noticed in larger SDS as compared to smaller ones, suggesting that photons survived at detectors had traveled wider within the medium with larger SDS. Thus, under the circumstances of trying to obtain focal changes in cerebral hemodynamics, the recommended SDS range in this study is especially more favorable than larger SDS options.

8640648, 2019, 11, Downloaded from https://onlinelibrary.wiley.com/doi/10.1002/jbio.201900175 by Drexel University, Wiley Online Library on [19/12/2023]. See the Terms and Conditions (https://onlinelibrary.wiley.com/terms

and-conditions) on Wiley Online Library for rules of use; OA articles are governed by the applicable Creative Commons License

4.6 | Study limitations

In this article, we modeled the adult head as a layered slab medium in an MC simulation. A more complex structure could be introduced and studied in the future by considering the true head curvature, with spatially varying thickness of extracerebral tissue and sulci and gyri of the brain tissue. In addition, optical properties in this study were chosen for a wavelength of 690 nm. Parameters for relatively longer wavelength selections should be investigated in future analysis, as well as various scattering coefficients of the brain tissue, considering the large variation of the scattering coefficient of brain tissue provided in previous reports [44, 62–65]. Another limitation of the study is the clinical model used in MC simulation. We simulated cerebral hematoma in different sizes; however, in real clinical cases, injured brains may have lesions such as perihematomal edema or cerebral edema. These more realistic, clinical cases should be investigated in the future.

5 | CONCLUSIONS

In this article, we demonstrated NIRS system measurements in MC simulation with different SDS settings. Our MC simulation results on healthy, uninjured head models suggested that increasing the SDS past 20 mm increases sensitivity to brain tissue. MC simulation under clinical settings also suggested that NIRS measurement can only discriminate lesions at a certain depth beyond certain SDS separations. Hence, the larger the separation between the source and the detector, the more sensitive the measurements become to the brain tissue. However, the results also suggested that detected signal strength declines exponentially as SDS increases. Therefore, sensitivity should be balanced against signal strength in SDS selection in NIRS probe designs.

ACKNOWLEDGMENTS

The work reported here was run on hardware supported by Drexel's University Research Computing Facility. The authors are grateful to Dr. Baruch Ben Dor for the discussion and feedback. The authors also would like to thank Jesse Mark for his help with the manuscript.

CONFLICT OF INTEREST

The authors declare no potential conflict of interest.

AUTHOR BIOGRAPHIES

Please see Supporting Information online.

ORCID

Lei Wang https://orcid.org/0000-0003-4415-1268

Hasan Ayaz https://orcid.org/0000-0001-5514-2741

Meltem Izzetoglu https://orcid.org/0000-0002-1768-3384

REFERENCE

- [1] T. Marin, J. Moore, Adv. Neonatal Care. 2011, 11, 382.
- [2] Y. Ozaki, C. W. Huck, K. B. Bec, Near-IR Spectroscopy and its Applications Vol., Elsevier, Amsterdam 2017, p. 11.
- [3] M. Ferrari, V. Quaresima, Neuroimage 2012, 63, 921.
- [4] A. Villringer, Trends Neurosci. 1997, 20, 435.
- [5] M. A. Yücel, J. J. Selb, T. J. Huppert, M. A. Franceschini, D. A. Boas, Curr. Opinion Biomed. Eng. 2017, 4, 78.
- [6] H. Ayaz, M. Izzetoglu, K. Izzetoglu, B. Onaral, B. B. Dor, J. Biomed. Opt. 2019, 24, 051411.
- [7] A. Curtin, H. Ayaz, Jap. Psycholog. Res. 2018, 60, 374.
- [8] F. Scholkmann, S. Kleiser, A. J. Metz, R. Zimmermann, J. M. Pavia, U. Wolf, M. Wolf, *Neuroimage* 2014, 85, 6.
- [9] E. Okada, D. T. Delpy, Appl. Optics. 2003, 42, 2906.
- [10] G. E. Strangman, Z. Li, Q. Zhang, PLoS One. 2013, 8, e66319.
- [11] Q. Fang, Biomed. Optics Express. 2010, 1, 165.
- [12] E. Okada, D. T. Delpy, Appl. Optics. 2003, 42, 2915.
- [13] M. Niwayama, Y. Yamashita, Photon Migration in Tissue, Springer, Boston 2013, p. 21.
- [14] B. Wilson, G. Adam, Med. Phys. 1983, 10, 824.
- [15] P. Van der Zee, D. T. Delpy, Simulation of the Point Spread Function for Light in Tissue by a Monte Carlo Method, Springer, Boston 1987, p. 179.
- [16] Y. Hasegawa, Y. Yamada, M. Tamura, Y. Nomura, Appl. Optics. 1991, 30, 4515.
- [17] M. Hiraoka, M. Firbank, M. Essenpreis, M. Cope, S. Arridge, P. Van Der Zee, D. Delpy, *Phys. Med. Biol.* **1993**, *38*, 1859.
- [18] L. Wang, S. L. Jacques, L. Zheng, Comput. Methods Programs Biomed. 1995, 47, 131.
- [19] A. V. Gorshkov, J. Comput. Sci. 2012, 3, 498.
- [20] M. Hiraoka, M. Firbank, M. Essenpreis, M. Cope, S. R. Arridge, P. van der Zee, D. T. Delpy, Monte Carlo Simulation of Light Transport through Inhomogeneous Tissue, Vol. 1888, International Society for Optics and Photonics, Los Angeles 1993, p. 149.
- [21] C. Zhu, J. Biomed. Opt. 2013, 18, 050902.
- [22] S. Arridge, M. Schweiger, M. Hiraoka, D. Delpy, *Med. Phys.* 1993, 20, 299.
- [23] S. Brigadoi, R. J. Cooper, Neurophotonics. 2015, 2, 025005.
- [24] C.-K. Lee, C.-W. Sun, P.-L. Lee, H.-C. Lee, C. Yang, C.-P. Jiang, Y.-P. Tong, T.-C. Yeh, J.-C. Hsieh, *Opt. Express* 2005, *13*, 8339.
- [25] Y. Fukui, Y. Ajichi, E. Okada, Appl. Optics. 2003, 42, 2881.
- [26] T. Hayashi, Y. Kashio, E. Okada, Appl. Optics. 2003, 42, 2888.
- [27] S. Kohri, Y. Hoshi, M. Tamura, C. Kato, Y. Kuge, *Physiol. Meas.* 2002, 23, 301.
- [28] G. Gratton, C. R. Brumback, B. A. Gordon, M. A. Pearson, K. A. Low, M. Fabiani, *Neuroimage* 2006, 32, 1576.

of use; OA

by the applicable Creative Commons

10 of 10 JOURNAL OF WANG ET AL.

BIOPHOTONICS

- [29] T. Li, H. Gong, J. Biomed. Opt. 2011, 16, 045001.
- [30] F. Herold, P. Wiegel, F. Scholkmann, A. Thiers, D. Hamacher, L. Schega, *Neurophotonics*. 2017, 4, 041403.
- [31] M. Ferrari, L. Mottola, V. Quaresima, Can. J. Appl. Physiol. 2004, 29, 463.
- [32] F. Orihuela-Espina, D. Leff, D. James, A. Darzi, G. Yang, *Phys. Med. Biol.* 2010, 55, 3701.
- [33] J. León-Carrión, U. León-Domínguez, Functional near-Infrared Spectroscopy (fNIRS): Principles and Neuroscientific Applications., InTech, Rijeka 2012.
- [34] H. Koizumi, T. Yamamoto, A. Maki, Y. Yamashita, H. Sato, H. Kawaguchi, N. Ichikawa, Appl. Optics 2003, 42, 3054.
- [35] R. M. Mudra, A. Nadler, E. Keller, J. Biomed. Opt. 2006, 11, 044009.
- [36] A. Villringer, J. Planck, C. Hock, L. Schleinkofer, U. Dirnagl, Neurosci. Lett. 1993, 154, 101.
- [37] L. Wang, H. Ayaz, M. Izzetoglu, B. Onaral, Comput. Biol. Med. 2017, 89, 68.
- [38] A. Ghosh, C. Elwell, M. Smith, Anesthesia Analgesia. 2012, 115, 1373.
- [39] A. N. Sen, S. P. Gopinath, C. S. Robertson, *Neurophotonics*. 2016, 3, 031409.
- [40] A. R. Sonkaya, NeuroQuantology. 2018, 16, 87.
- [41] P. Schober, S. M. Bossers, L. A. Schwarte, *BioMed Res. Int.* 2017, 2017, 1846830.
- [42] S. Bressan, M. Daverio, F. Martinolli, F. Mario, I. P. Steiner, L. Da Dalt, *Childs Nerv. Syst.* 2014, 30, 477.
- [43] R. Francis, B. Khan, G. Alexandrakis, J. Florence, D. MacFarlane, *Biomed. Opt. Express* 2015, 6, 3256.
- [44] C. Bonnéry, M. Desjardins, P. Pouliot, F. Lesage, P.-O. Leclerc, R. D. Hoge, L. Bherer, J. Biomed. Opt. 2012, 17, 056002.
- [45] A. Young, T. Germon, N. Barnett, A. Manara, Br. J. Anaesth. 2000, 84, 38.
- [46] A. Adeloye, K. R. Kattan, F. N. Silverman, Am. J. Phys. Anthropol. 1975, 43, 23.
- [47] C. Mansouri, J.-P. L'Huillier, N. H. Kashou, A. Humeau, *Lasers Med. Sci.* 2010, 25, 431.
- [48] G. E. Strangman, Q. Zhang, Z. Li, Neuroimage 2014, 85, 136.
- [49] E. Okada, M. Firbank, M. Schweiger, S. R. Arridge, M. Cope, D. T. Delpy, *Appl. Optics* **1997**, *36*, 21.
- [50] H. Sorvoja, T. Myllylä, M. Y. Kirillin, E. A. Sergeeva, R. A. Myllylä, A. Elseoud, J. Nikkinen, O. Tervonen, V. Kiviniemi, *Quantum Electronics*. 2010, 40, 1067.
- [51] J. Selb, T. M. Ogden, J. Dubb, Q. Fang, D. A. Boas, J. Biomed. Opt. 2014, 19, 016010.

- [52] A. Machado, Z. Cai, G. Pellegrino, O. Marcotte, T. Vincent, J. Lina, E. Kobayashi, J. Neurosci. Methods 2018, 309, 91.
- [53] E. Sakakibara, F. Homae, S. Kawasaki, Y. Nishimura, R. Takizawa, S. Koike, A. Kinoshita, H. Sakurada, M. Yamagishi, F. Nishimura, *Neuroimage* 2016, 142, 590.
- [54] T. Funane, H. Atsumori, T. Katura, A. N. Obata, H. Sato, Y. Tanikawa, E. Okada, M. Kiguchi, *Neuroimage* 2014, 85, 150.
- [55] T. Yamada, S. Umeyama, K. Matsuda, PLoS One. 2012, 7, e50271.
- [56] P. Eggenberger, M. Wolf, M. Schumann, E. D. de Bruin, Frontiers in Aging Neuroscience 2016, 8, 66.
- [57] K. L. Koenraadt, E. G. Roelofsen, J. Duysens, N. L. Keijsers, Neuroimage 2014, 85, 415.
- [58] L. Gagnon, R. J. Cooper, M. A. Yücel, K. L. Perdue, D. N. Greve, D. A. Boas, *Neuroimage* 2012, 59, 2518.
- [59] C.-y. Liang, Y. Yang, C.-s. Shen, H.-j. Wang, N.-M. Liu, Z.-w. Wang, F.-l. Zhu, R.-x. Xu. Military Med. 2018, 183, e318.
- [60] R. Lazarus, K. Helmick, S. Malik, E. Gregory, Y. Agimi, D. Marion, Neurosurg. Focus 2018, 45, E15.
- [61] H. Ayaz, B. B. Dor, D. Solt, B. Onaral, J. Med. Dev. 2011, 5, 027540.
- [62] G. Strangman, M. A. Franceschini, D. A. Boas, *Neuroimage* 2003, 18, 865.
- [63] Y. Zhang, J. Sun, J. Modern Optics. 2010, 57, 2159.
- [64] Y. Sakakibara, K. Kurihara, E. Okada, Optical Review. 2016, 23, 346.
- [65] W.-F. Cheong, S. A. Prahl, A. J. Welch, *IEEE J. Quant. Electron.* 1990, 26, 2166.

SUPPORTING INFORMATION

Additional supporting information may be found online in the Supporting Information section at the end of this article.

How to cite this article: Wang L, Ayaz H, Izzetoglu M. Investigation of the source-detector separation in near infrared spectroscopy for healthy and clinical applications. *J. Biophotonics*. 2019;12: e201900175. https://doi.org/10.1002/jbio.201900175